Electronic Supplementary Material (ESI) for Chemical Science.

Supplementary Information

Chunwei Hsu,[†,#] Werner M. Schosser,[‡,#] Patrick Zwick,[¶,#] Diana Dulić,[§] Marcel Mayor,[*,¶] Fabian Pauly,[*,‡] and Herre S. J. van der Zant[*,†]

†*Kavli Institute of Nanoscience, Delft University of Technology, Lorentzweg 1, Delft 2628 CJ, The Netherlands*

‡*Institute of Physics, University of Augsburg, 86135 Augsburg, Germany*

¶*Department of Chemistry, University of Basel, St. Johanns-Ring 19, 4056 Basel, Switzerland*

§*Department of Physics, Department of Electrical Engineering, Faculty of Physical and Mathematical Sciences, University of Chile, Avenida Blanco Encalada 2008, Santiago 8330015, Chile*

‖*Institute for Nanotechnology (INT), Karlsruhe Institute of Technology (KIT), P.O. Box 3640, 76021 Karlsruhe, Germany*

⊥*Lehn Institute of Functional Materials (LIFM), School of Chemistry, Sun Yat-Sen University (SYSU), 510275 Guangzhou, China*

#*These authors contributed equally.*

E-mail: marcel.mayor@unibas.ch; fabian.pauly@uni-a.de; H.S.J.vanderZant@tudelft.nl

Contents

SI.1 Experiment

SI.1.1 MCBJ Setup

We study single cofacial porphyrin molecules with a MCBJ setup. The schematic of the setup is shown in Fig. S1. To fabricate the MCBJ sample, we follow lithography procedures described in previous reports.[1,2] First, we spin-coat a polyimide (PI) insulating layer on a flexible phosphor bronze (PB) substrate. Next we use MMA/PMMA double-layer resist and perform electron-beam lithography to define the electrode patterns. After the development of the lithographically-defined patterns, we deposit a layer of gold at a thickness of 80 nm on top of a 3 nm thick titanium adhesive layer with electron-beam evaporation. After the lift-off process of resist, we use an oxygen plasma to create an under-cut for suspending the nano-constriction.

To characterize single molecules electrically, the sample is mounted onto the MCBJ setup. In a fast-breaking measurement a constant voltage is supplied across the junction, while the current is monitored by a homemade logarithmic current amplifier. Simultaneously, a piezo element is pushing the central support of the MCBJ setup vertically to induce a horizontal displacement of the electrodes. By bending and unbending the MCBJ substrate, thousands of fast-breaking conductance traces are obtained for statistical analysis. Before the deposition of the molecule of interest, a reference fast-breaking measurement is performed on the clean MCBJ sample. Afterwards, a solution of ZnPC2 or 2HPC2 molecules in dichloromethane with concentrations from 5 to 100 μM is drop-cast onto the MCBJ sample for single-molecule characterization.

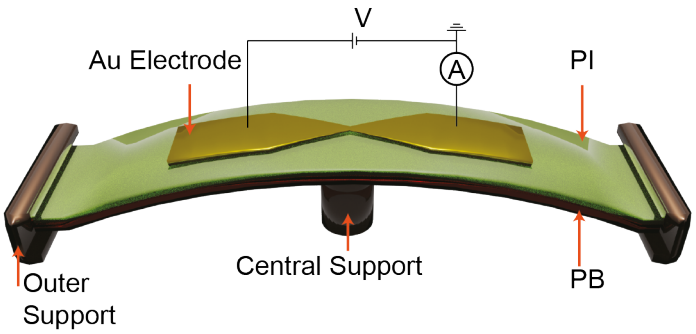

Figure S1: Schematic of the employed MCBJ setup.

SI.1.2 Additional Fast-Breaking Measurements of ZnPC2

Additional fast-breaking measurements of ZnPC2 on a different sample are displayed in Figs. S2 and S3 for bias voltages of 250 mV and 100 mV, respectively. In Figs. S2a and S3a the two-dimensional (2D) conductance-displacement histograms are plotted without any data selection. In both cases a conductance plateau located at around $2 \times 10^{-6} G_0$ is observed, consistent with the 2D histogram shown in Fig. 2 of the main text. Individual fast-breaking traces are plotted in Figs. S2b and S3b. These example traces feature a conductance minimum around an electrode displacement of 1.5 nm, then an increase of conductance followed by a plateau region that lasts about 1 nm, before the conductance decays exponentially and the contact finally breaks. These findings are consistent with the results reported in the main text.

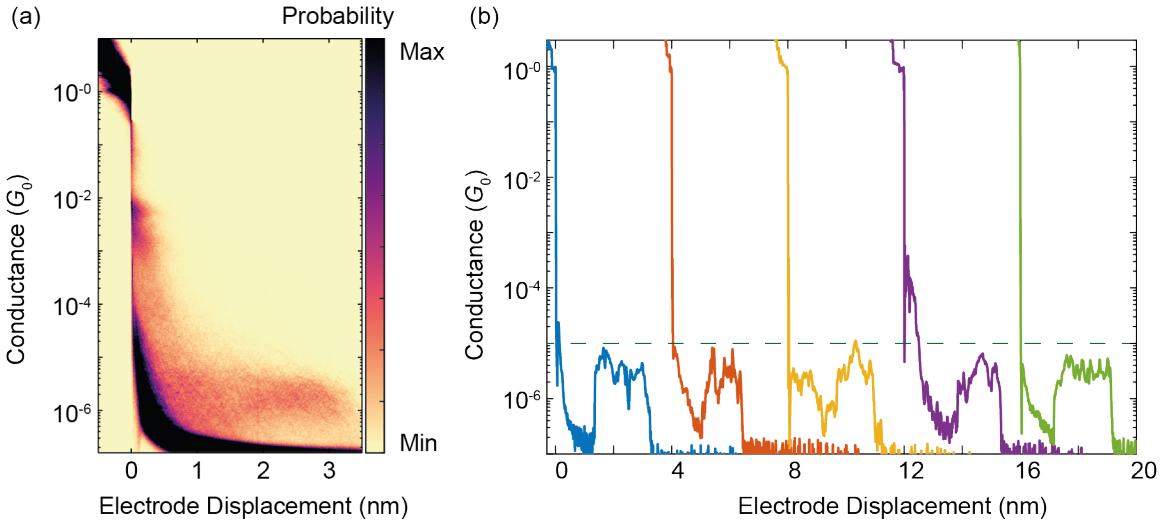

Figure S2: (a) Additional ZnPC2 fast-breaking measurements of sample 2 at an applied bias voltage of 250 mV. 10,000 conductance traces are compiled in the 2D conductance vs. displacement density plot. (b) Five example traces, showing large conductance variations of up to two orders of magnitude. The horizontal dashed line at $G = 10^{-5} G_0$ is a guide to the eye.

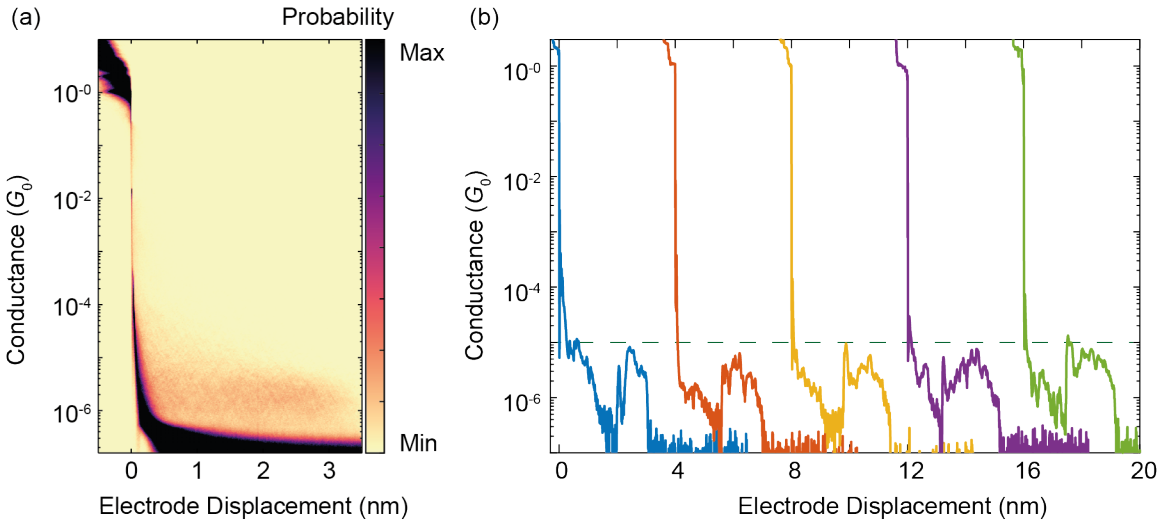

Figure S3: Same as Fig. S2 but at an applied bias voltage of 100 mV.

SI.1.3 Remainder Classes of Fast-Breaking Measurements of ZnPC2

In Fig. 2 of the main text, a reference-free clustering algorithm is used to extract the molecular traces.[3] We choose a total of five classes for the clustering algorithm, and the first class, containing the relevant molecular traces, is shown in Fig. 2b. For completeness, the reminder classes are displayed in Fig. S4. Classes 3, 4 and 5 only show direct tunneling-like features, where the conductance decreases exponentially as a function of displacement and where no conductance plateau is observed. Class 2 however contains some traces with additional features, in particular traces with a displacement length shorter than 2 nm. We assign these short traces to breaking events, where the molecules are not fully extended.

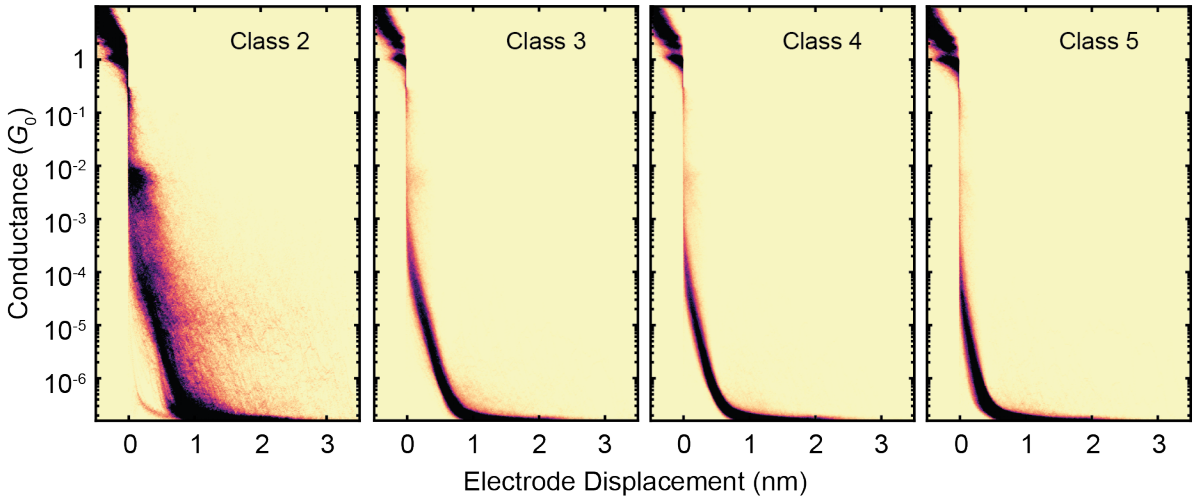

Figure S4: Remainder classes for Fig. 2a from the reference-free clustering algorithm. As described in the main text, the applied bias voltage amounts to 250 meV.

SI.1.4 Fast-Breaking Measurements of 2HPC2

In addition to the ZnPC2 molecule of Fig. 1, we have characterized the free-base cofacial porphyrin 2HPC2. The chemical structure is shown in Fig. S5.

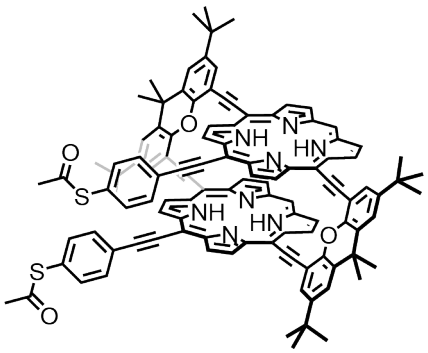

Figure S5: Chemical structure of 2HPC2.

Fast-breaking measurements at bias voltages of 250 mV and 100 mV are displayed in Figs. S6 and S7, respectively. Similar to ZnPC2, the 2D conductance-displacement histograms of 2HPC2 show a molecular conductance value of around $2 \times 10^{-6} G_0$, see Figs. S6a and S7a. Individual fast-breaking traces are plotted in Figs. S6b and S7b. These traces feature the same behavior as ZnPC2, following the four conductance regimes, described by the DFT calculations. The similarities suggest that the transport mechanism is the same for 2HPC2 and ZnPC2. Thus the metal center has little effect on the electronic transport in the cofacial porphyrin, consistent with previous studies.[4]

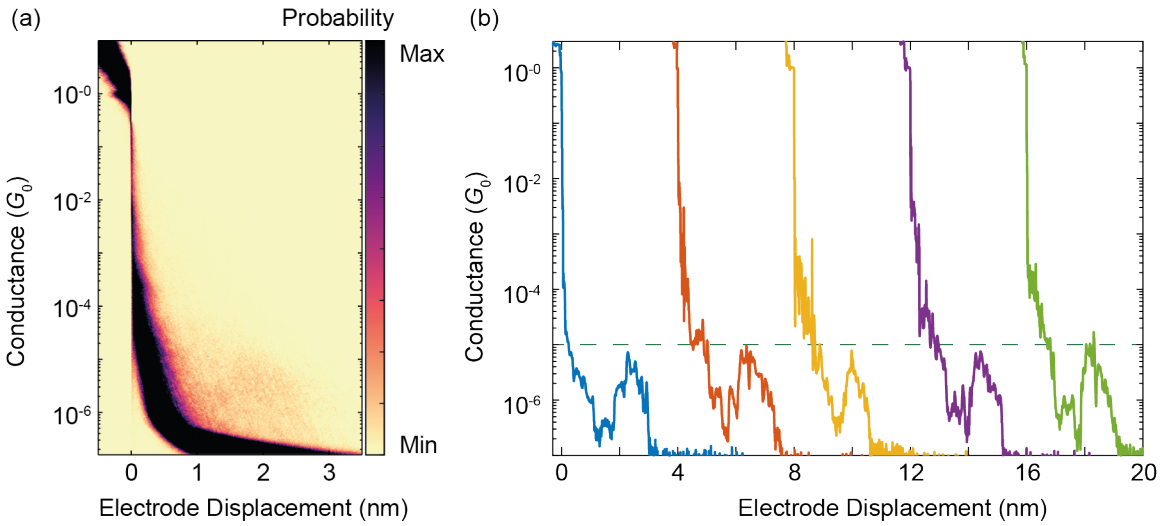

Figure S6: (a) Fast-breaking measurements on 2HPC2, measured at a bias voltage of 250 mV. The 2D conductance histogram consists of 7,589 conductance-displacement traces. (b) Five example traces, offset by hand by 4 nm, showing the large conductance variations, which are similar to the case of ZnPC2.

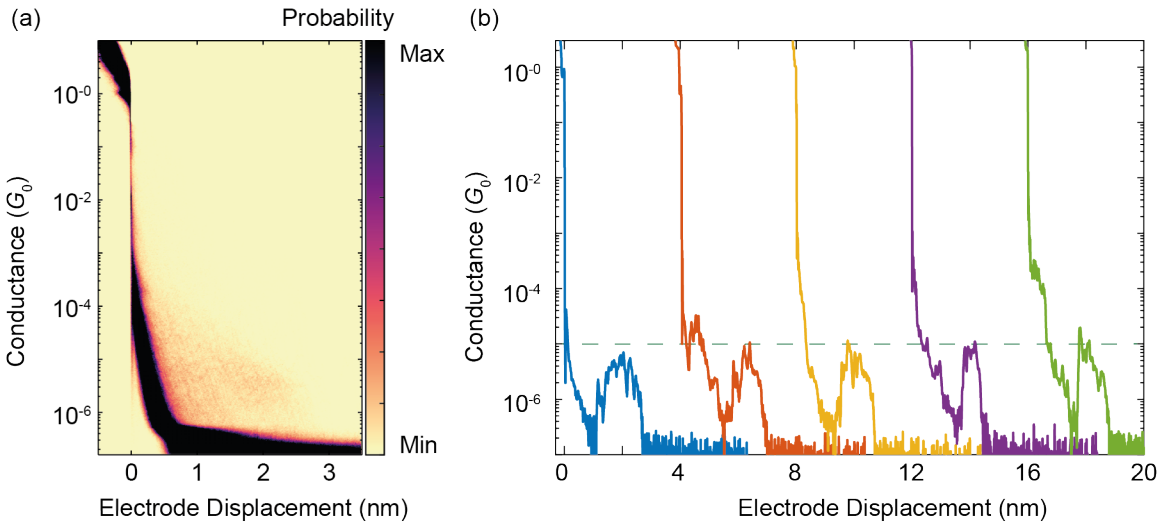

Figure S7: Same as Fig. S6 but at a bias voltage of 100 mV. The density plot now comprises 9,225 conductance-distance traces.

SI.1.5 Gauge Factor Analysis

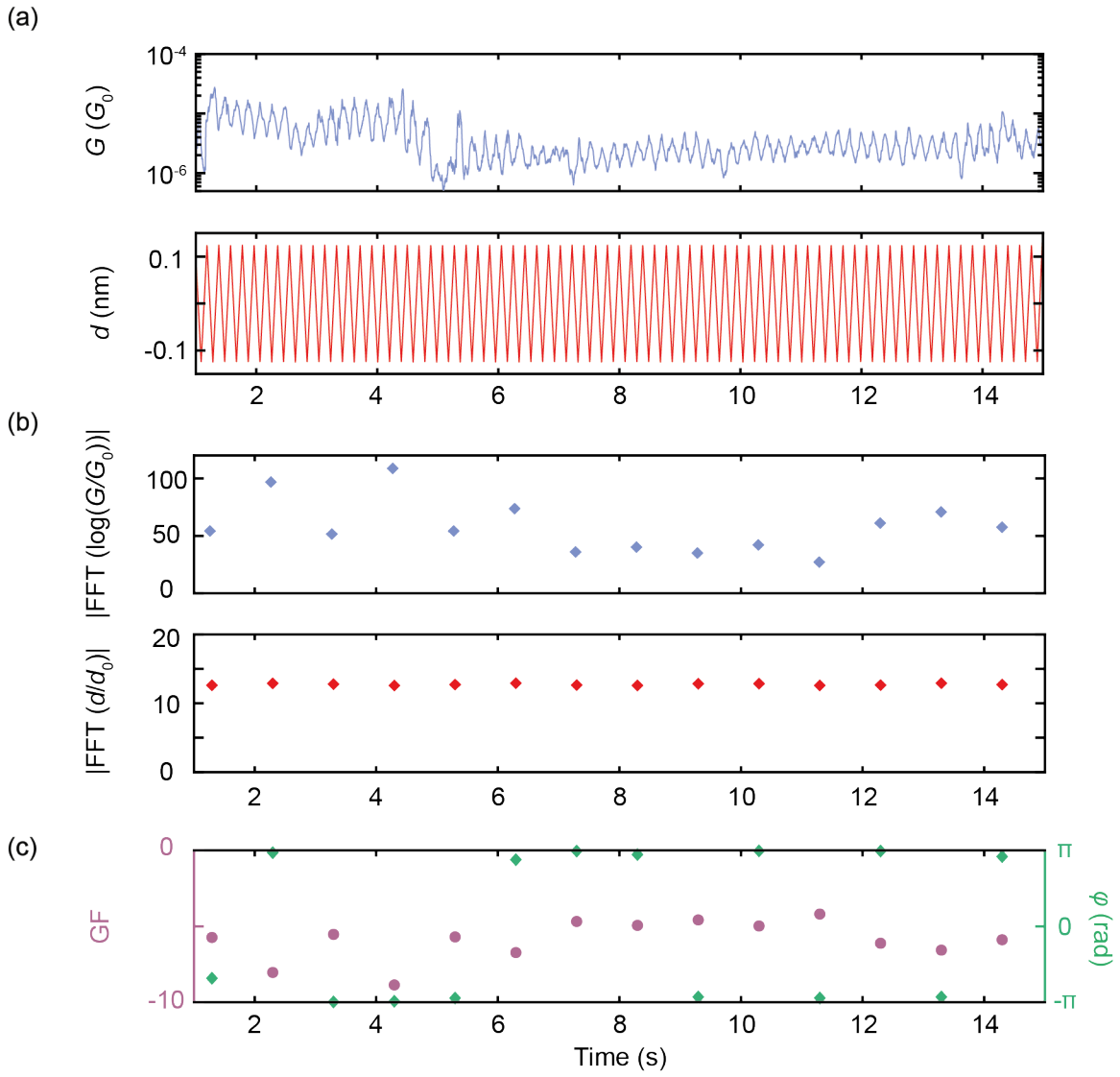

Figure S8: GF analysis. (a) Raw data of an electrode displacement modulation measurement. The top panel shows the conductance trace as a function of time, and the bottom panel displays the modulated electrode displacement as a function of time. The modulation amplitude is 2.5 Å. (b) Raw data after the FFT. The top panel visualizes the FFT amplitude of $\log(G/G_0)$ and the bottom panel is the FFT amplitude of d/d_0. Both FFT amplitudes are evaluated at the driving frequency $f = 5$ Hz. (c) GFs and phases of the example data. The GF and phase φ are obtained by taking the ratio of FFT amplitudes shown in panel (b), see Eqs. (S1) and (S2).

The displacement modulation measurements, described in the main text of this work, provide a means to study the conductance response of the single-molecule junctions around

a selected initial electrode displacement. The general procedure of the statistical gauge factor (GF) analysis is explained in Fig. S8. We take the raw signals of conductance and displacement as a starting point, see Fig. S8a. Next we perform a fast Fourier transform (FFT) on the two signals, $\log(G/G_0)$ and d/d_0, for every five cycles of the driving signal. Here, G is the conductance, G_0 is the quantum of conductance $G_0 = 2e^2/h$, d is the electrode displacement, and d_0 is the average length of a single-molecule plateau, as determined from the fast-breaking measurements. To illustrate, how the FFT affects the two input signals, the absolute values of the results are visualized in Fig. S8b. Then, we take the ratio of the two FFT results, which gives the complex number

$$z(f) = r(f)e^{i\varphi(f)} = \frac{\mathrm{FFT}(\log(G/G_0))(f)}{\mathrm{FFT}(d/d_0)(f)} \tag{S1}$$

with a corresponding frequency-dependent amplitude $r(f)$ and phase $\varphi(f)$. Finally, we define

$$\mathrm{GF} = r(f) \times s, \tag{S2}$$

with

$$s = \begin{cases} 1, & \text{if } |\varphi(f)| \leq \pi/2, \\ -1, & \text{if } |\varphi(f)| > \pi/2, \end{cases} \tag{S3}$$

where the phase is assumed to take values in the interval $\varphi(f) \in [-\pi, \pi]$, see also Fig. S8, and $f = 5$ Hz is chosen to be the driving frequency of our displacement modulation experiment. Therefore, the GF is positive, if the two signals are in phase, and negative, if they are out of phase.

Let us consider Fig. 3a as an example. The GF is predominantly negative, suggesting an anti-phase relation between G and d. This means that if the electrode displacement increases at this initial electrode displacement position, the conductance typically goes down, which is in agreement with the trends observed in Fig. 2.

SI.2 Theory

SI.2.1 Relation between Conduction Properties and Junction Geometry

In the main text we discuss, how the different conductance regions are related to the complex molecular motion inside the junction. To establish this relation in greater detail, we analyze here the transmission as a function of energy at different electrode displacements d, as shown in Fig. S9. The transmission curves correspond to vertical cuts in Fig. 5b of the main text. In addition, we study several intramolecular and molecule-electrode distances during the pulling, as visible in Fig. S10. In particular, Fig. S10a quantifies the separation of the benzene-ethynly-porphyrin decks at various points along the central molecular axis, Fig. S10b reveals possible asymmetric separations of the porphyrins, and Fig. S10c specifies rotations of benzene linkers with regard to the gold electrode. In order to establish a close connection, we will discuss Figs. S9 and S10 simultaneously.

The fast initial conductance decay in region (i), c.f. Fig. 5a in the main text, is related to the vanishing of a direct tunneling contribution in this region. Figure S9a shows the clear decay of an energy-independent background of the transmission inside the HOMO-LUMO gap. Figure S10a shows that the decay is caused by the separation of ethynylbenzenethiol linkers, while the porphyrins stay close together at this stage. The transmission eigenchannels in Fig. 6a and 6b of the main text corroborate these statements further, since they show the vanishing of the direct tunneling contributions between ethynyl-benzenes. Effects of rotational motions of both benzenethiol anchors, see Fig. S10c, are basically hidden in the large conductance changes caused by the direct tunneling contributions.

Figure S9b characterizes region (ii) by a constant position of transmission resonances, which appear at molecular orbital energies, whose energetic broadening changes. Region (ii) starts and ends with fast rotations of left and right anchoring benzene rings at $d = 4.4$ Å and 7.8 Å respectively, which consecutively align favorably to the pulling direction, as Figure S10c

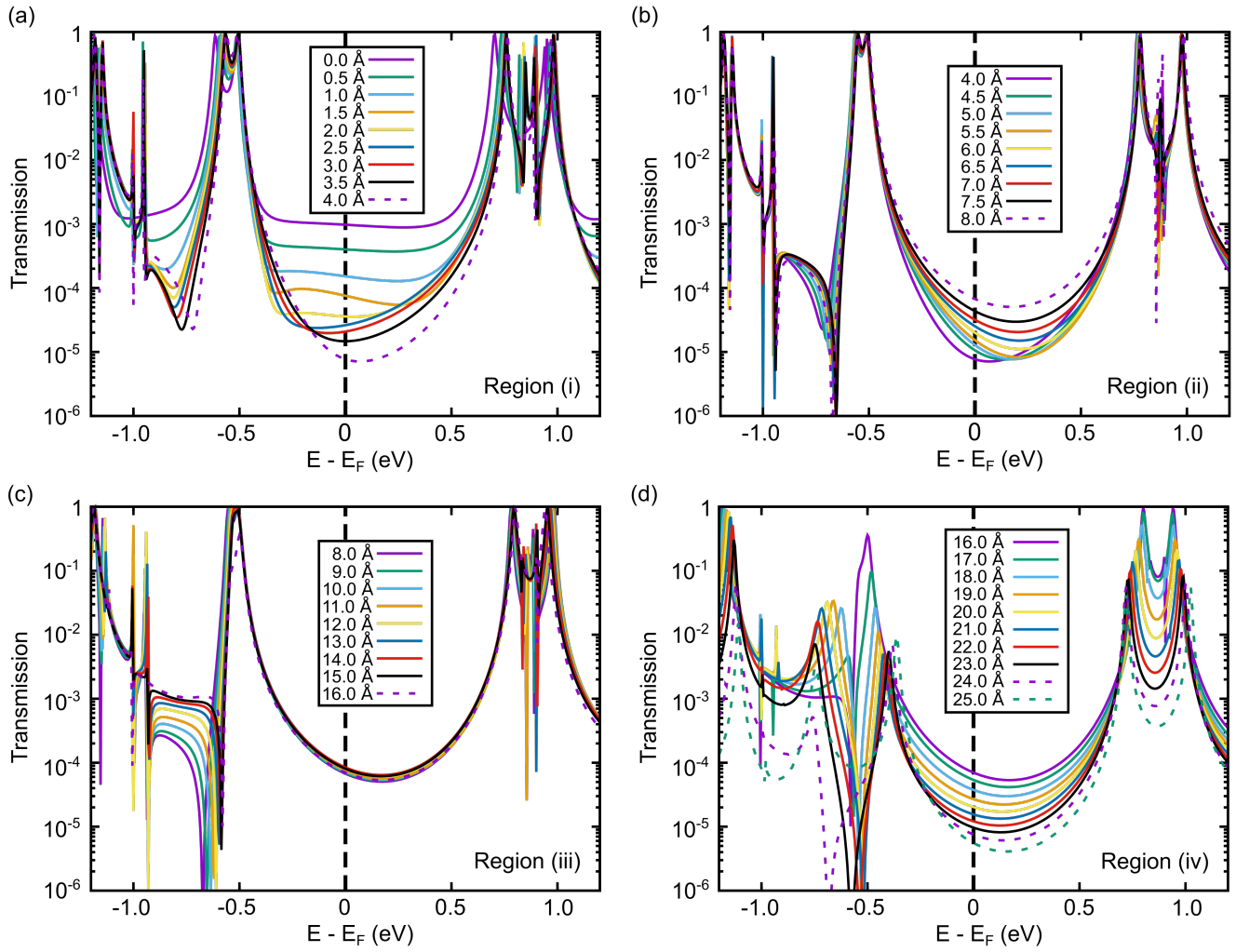

Figure S9: (a)-(d) Transmission as a function of energy for various electrode displacements, grouped according to the four conductance regions (i) to (iv) introduced in the main text. The curves are obtained as vertical cuts in the transmission map of Fig. 5b for the simulated Au-ZnPC2-Au junction.

reveals. These fast movements also lead to dips in the tensile force in Fig. 5a of the main text, whereas other atom movements are less abrupt. As Fig. S10 shows, the increasing conductance in region (ii) is due to a combined effect. On the one hand the two porphyrins in the upper part of the molecule are pressed together, see the orange, yellow and dark blue lines in Fig. S10a and the light blue, orange and yellow ones in Fig. S10b. On the other hand, while the interaction area between the porphyrins remains almost constant, a growing electronic coupling between the para-ethynylbenzenethiols and the porphyrins leads to a

further broadening of the transmission resonances. Note that the benzene rings of the two ethynylbenzenes behave differently. Since the xanthene bridges are tilted, porphyrin planes cannot align perfectly on top of each other but are shifted in the molecular ground state geometry, and so are the benzene rings, see Figs. 1a and 4a of the main text. For this reason, the left benzene ring in our junctions is rather free already at the beginning of the pulling process, while the one on the right is a bit more restricted by the presence of the other deck and hence rotates typically at larger electrode displacements.

In region (iii) the energy-dependent transmission curves in Fig. S9c remain basically unchanged inside the HOMO-LUMO gap for different electrode displacements. This leads to the plateau in the conductance visible in Fig. 5a of the main text. In this region the porphyrins are separating, starting from the molecule's lower part, c.f. the orange and yellow curves in Fig. S10a and the purple, green and light blue curves in Fig. S10b. In contrast the upper part of the porphyrin double decker is compressed further, c.f. the dark blue curve in Fig. S10a and the orange and yellow curves in Fig. S10b. The peeling off and the further compression counteract, combining to a rather constant conductance in region (iii).

The fast exponential decrease of the conductance with respect to d in region (iv) is clearly reflected in the transmission curves of Fig. S9d. At the electrode displacement of about $d = 15$ Å, all twists and distortions within the molecule are basically removed due to the tensile strain of the stretching process. This is also visible in Fig. S10c, where distances between the Au tip atoms and the carbon atoms of the benzene rings on each side are very similar starting from that distance. Further separation of the electrodes thus reduces the region of porphyrin-porphyrin overlap. As all parts of the two molecular decks of the cofacial porphyrins separate, including now also the the upper part of the "porphyrin press", c.f. the dark blue curve in Fig. S10a and the orange and yellow curves in Figure S10b, the conductance decays quickly. Ultimately, the maximum separation of the porphyrins is limited by the covalent xanthene bridges, which are not displayed in the junction geometries of Fig. S10 however to improve the visibility of the studied atomic distances.

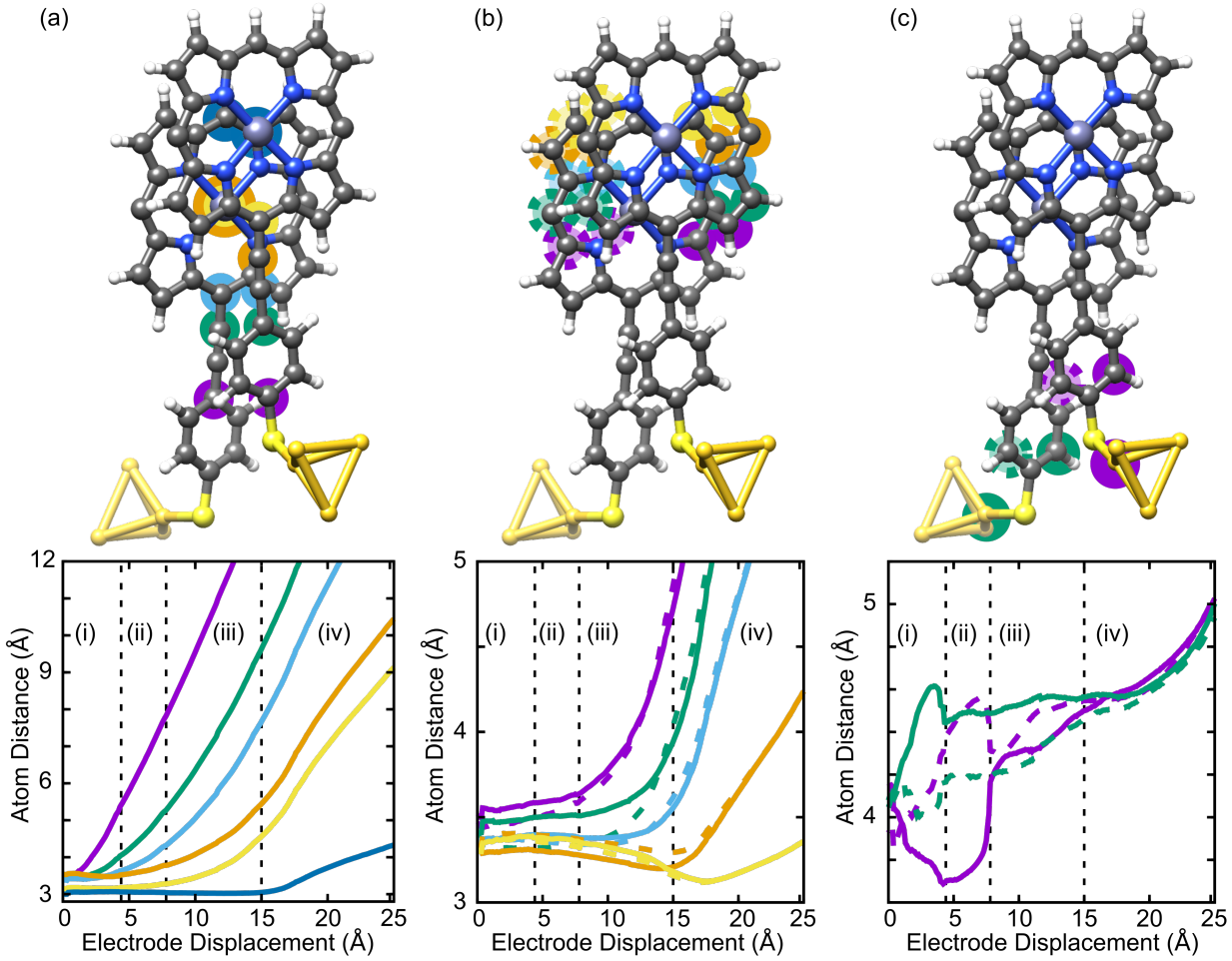

Figure S10: Evolution of atomic separations as a function of electrode displacement in the simulated stretching junction process. For better visibility, we removed xanthene bridges and acetylene joints in the ball-and-stick representations. Distances are determined between identically colored atoms, plotted with a line of the same color and linestyle. (a) Distances between atoms on the central molecular backbone. (b) Comparison of atomic separations in left and right parts of the porphyrin stack. (c) Distance from the marked carbon atoms of the benzene linker to their respective nearest electrode gold atom, quantifying rotational motion in regions (i) to (iii), while an increase of bond distances prevails in region (iv).

SI.2.2 Robustness of the Conductance with Regard to Temperature Changes

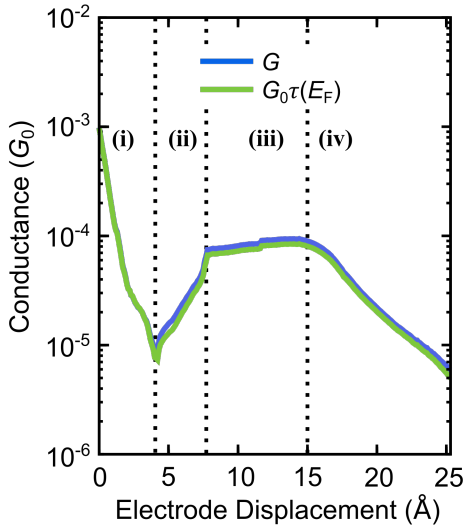

Figure S11: Conductance as a function of electrode displacement. The conductance is shown at room temperature $T = 300$ K (solid blue line, G) and in the low-temperature limit (solid green line, $G_0\tau(E_F)$). Vertical dotted lines separate the four characteristic conductance regions: (i) exponential decrease, (ii) exponential increase, (iii) plateau, and (iv) exponential decrease.

As presented in the main text, we compute the conductance at room temperature via the linear response expression

$$G = G_0 \int_{-\infty}^{\infty} dE \left(-\frac{\partial f(E)}{\partial E} \right) \tau(E). \tag{S4}$$

Here $\tau(E)$ is the energy-dependent transmission function and $f(E)$ the Fermi function. For sufficiently low temperatures, Eq. (S4) simplifies to $G \approx G_0\tau(E_F)$ and thus establishes a direct connection to the calculated transmission map in Fig. 5b of the main text. Following the Fermi energy in Fig. 5b, marked by the horizontal dashed line, yields the low temperature conductance, shown as the solid green line in Fig. S11. Comparing G and $G_0\tau(E_F)$ in Fig. S11 reveals that the conductance is very stable with regard to changes in temperature, demonstrating its robustness in the regions (i)-(iv).

SI.2.3 Relation between Bending and Geometric Alignment of Benzene and Porphyrin Rings

Let us study in greater detail the origin of the rotational motion of the benzene rings during the stretching process, see Fig. S10c, especially in regions (i) and (ii). Each deck of the PC2 molecule consists of an ethynylbenzenethiol coupled to a porphyrin. This means that the sp^2-hybridized conjugated electron systems of the benzene ring and of the porphyrin are connected covalently through an sp-hybridized carbon-carbon triple bond of the ethynylene. As a simplified toy model we consider diphenylacetylene, which features a similar sequence of sp^2-sp-sp^2 electron systems.

The energetics of diphenylacetylene with regard to bending and ring rotations are shown in Fig. S12. Figure S12a displays the behavior of the total DFT energy, if the right benzene ring is rotated at different bending levels. We quantify the bending of the diphenylacetylene by the sulfur-sulfur distance $d - d_{\max}$, with $d_{\max} = 13.2$ Å being the distance of a fully optimized planar diphenylacetylene. We observe that for all $d - d_{\max}$ the molecular energy rises monotonically with the benzene's rotation angle, reaching a maximum at 90°. Figure S12b shows that the total energy of the molecule in the configuration without ring rotation rises rather linearly with decreasing $d - d_{\max}$ or increasing flexure. Importantly, the energy barrier $\Delta E = E(90°) - E(0°)$ for rotation of one of the molelcule's benzenethiols grows for larger bending of the molecule. This means that the energy gained by reducing the torsion angle between the terminal sp^2 hybridized aromatic systems increases the more the structure is bent, or in other words, the forces aiming for a reduced torsion angle increase by bending the structure.

Let us now apply these insights to the motion of the PC2 molecule in the regions (i) and (ii). At the start of the stretching process, the left ethynylbenzene linker separates from the rest of the molecule. With increasing separation the benzene ring rotates to maximize the π-orbital coupling with the opposite deck in a sliding fashion. Continuing the pulling and reducing the through-space interaction between the lower parts of the decks at the ethynyl-

benzene linkers further, the ethynyl bridge is bending more and more. This implies that a "parallel" alignment of the π-systems of the benzene and porphyrin becomes increasingly favored. Finally, the left linker rearranges by rotating the benzenethiol backwards to a configuration with small rotation angle. The same process occurs for the right benzene linker but happens later in the stretching process, reflecting the inequivalence of the benzene rings due to the initial shift between the two decks, discussed in section SI.2.1.

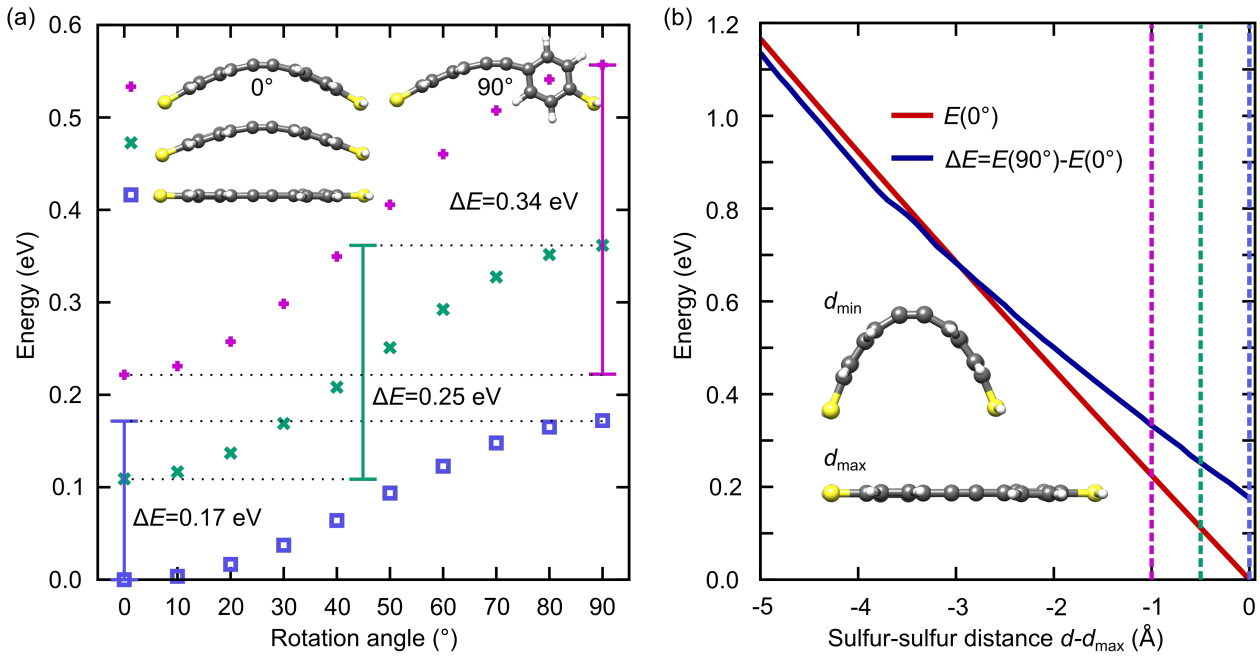

Figure S12: (a) Total DFT energy as a function of the rotation angle of the diphenylacetylene's right benzenethiol ring for the sulfur-sulfur distances of $d-d_{\max} = 0.0$ Å (blue), -0.5 Å (green) and -1.0 Å (pink), indicating a higher rotational energy barrier for a stronger bending. (b) Total DFT energy of the configuration without ring rotation (red line) and rotational energy barrier ΔE as a function of the sulfur-sulfur distance $d - d_{\max}$ (blue line). The vertical dashed lines mark the three distances, for which the energy dependence as a function of rotation angle is studied in detail in panel (a).

SI.3 Synthesis

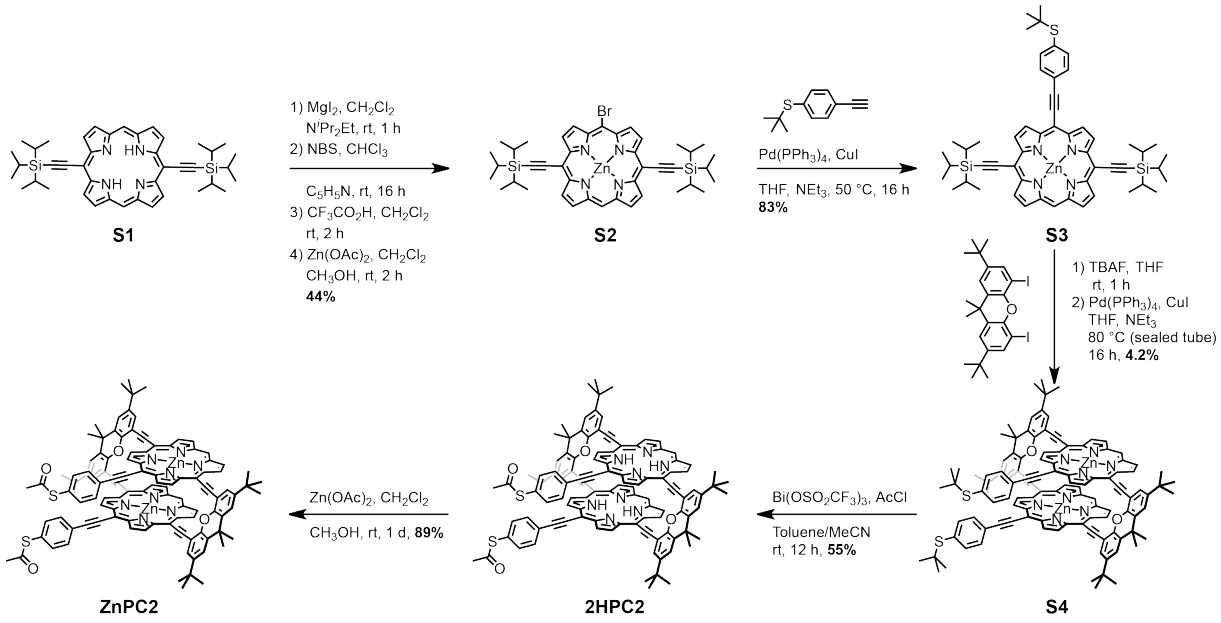

Figure S13: Synthetic overview.

The herein investigated structures 2HPC2 and ZnPC2 were synthesized and characterized as described in detail previously.[5] A metalation and de-metalation procedure, combining statistical bromination of S1, afforded the asymmetric porphyrin precursor S2, see Fig. S13. Subsequent palladium mediated Sonogashira cross coupling with the anchoring group bearing phenyl ethynylene yielded the key intermediate of the synthesis, S3. Liberation of the free acetylenes enabled four-fold Sonogashira macrocyclization yielding S4, under high dilution conditions. Bismuth triflate promoted trans-protection of the thioethers to thioacetates gave the compound of interest, 2HPC2, which almost quantitatively undergoes metalation to afford ZnPC2.

References

1. Martin, C. A.; Ding, D.; van der Zant, H. S. J.; van Ruitenbeek, J. M. Lithographic mechanical break junctions for single-molecule measurements in vacuum: possibilities

and limitations. *New Journal of Physics* **2008**, *10*, 065008.

2. Martin, C. A.; Smit, R. H. M.; van Egmond, R.; van der Zant, H. S. J.; van Ruitenbeek, J. M. A versatile low-temperature setup for the electrical characterization of single-molecule junctions. *Review of Scientific Instruments* **2011**, *82*, 053907.

3. Cabosart, D.; El Abbassi, M.; Stefani, D.; Frisenda, R.; Calame, M.; van der Zant, H. S. J.; Perrin, M. L. A reference-free clustering method for the analysis of molecular break-junction measurements. *Applied Physics Letters* **2019**, *114*, 143102.

4. El Abbassi, M.; Zwick, P.; Rates, A.; Stefani, D.; Prescimone, A.; Mayor, M.; van der Zant, H. S. J.; Dulić, D. Unravelling the conductance path through single-porphyrin junctions. *Chemical Science* **2019**, *10*, 8299–8305.

5. Zwick, P.; Hsu, C.; El Abbassi, M.; Fuhr, O.; Fenske, D.; Dulić, D.; van der Zant, H. S. J.; Mayor, M. Synthesis and Transport Studies of a Cofacial Porphyrin Cyclophane. *The Journal of Organic Chemistry* **2020**, *85*, 15072–15081.